nature COMMUNICATIONS

ARTICLE

DOI: 10.1038/s41467-018-07124-x OPEN

Magnetic field compatible circuit quantum electrodynamics with graphene Josephson junctions

J.G. Kroll[1], W. Uilhoorn[1], K.L. van der Enden[1], D. de Jong[1], K. Watanabe[2], T. Taniguchi[2], S. Goswami[1], M.C. Cassidy[1] & L.P. Kouwenhoven[1,3]

Circuit quantum electrodynamics has proven to be a powerful tool to probe mesoscopic effects in hybrid systems and is used in several quantum computing (QC) proposals that require a transmon qubit able to operate in strong magnetic fields. To address this we integrate monolayer graphene Josephson junctions into microwave frequency superconducting circuits to create graphene based transmons. Using dispersive microwave spectroscopy we resolve graphene's characteristic band dispersion and observe coherent electronic interference effects confirming the ballistic nature of our graphene Josephson junctions. We show that the monoatomic thickness of graphene renders the device insensitive to an applied magnetic field, allowing us to perform energy level spectroscopy of the circuit in a parallel magnetic field of 1 T, an order of magnitude higher than previous studies. These results establish graphene based superconducting circuits as a promising platform for QC and the study of mesoscopic quantum effects that appear in strong magnetic fields.

[1] QuTech and Kavli Institute for Nanoscience, Delft University of Technology, 2600 GA Delft, The Netherlands. [2] Advanced Materials Laboratory, National Institute for Materials Science, 1-1 Namiki, Tsukuba 305-0044, Japan. [3] Microsoft Station Q Delft, 2600 GA Delft, The Netherlands. Correspondence and requests for materials should be addressed to L.P.K. (email: Leo.Kouwenhoven@Microsoft.com)

A superconducting transmon qubit[1] resilient to strong magnetic fields is an important component for proposed topological[2–4] and hybrid quantum computing (QC) schemes[5,6]. A transmon qubit consists of a Josephson junction (JJ) shunted by a large capacitance, coupled to a high quality factor superconducting resonator. In conventional transmon devices, the resonator is fabricated from Al and the JJ is fabricated from an Al/AlO$_x$/Al tunnel junction[1], both of which cease operation above the critical magnetic field of bulk Al, ~10 mT. Even when considering alternative type II superconductors such as NbTiN or MoRe that can sustain superconductivity beyond $B = 8$ T[7], when subjected to a strong magnetic field the superconductor will experience detrimental effects such as reduction of the superconducting gap, increased quasiparticle generation[8] and the formation of Abrikosov vortices that cause resistive losses in a microwave field. In addition to disrupting the superconductivity, magnetic flux penetrating the JJ produces electron interference effects that reduce the Josephson energy E_J and strongly suppress the transmon energy spectrum. If the transmon is to be used for fast quantum gates, fast charge-parity detection and long range quantum state transfer in QC schemes[3,9,10] we are compelled to consider alternatives to conventional Al based JJs. Proximitised semiconducting nanowires, acting as gate-tuneable superconductor-normal-superconductor JJs[11] have been used successfully in a variety of microwave frequency superconducting circuits, allowing for studies of Andreev bound states[12,13], electrically tuneable transmon qubits[14,15] and transmons that exhibit substantial field compatibility[16]. Graphene JJs are an attractive alternative as they exhibit ballistic transport, high critical currents[7,17,18] and the atomic thickness of the graphene junction greatly reduces flux penetration, protecting the JJ from orbital interference effects that would suppress E_J in high parallel fields. When combined with geometric techniques that protect the superconducting film, such as critical field enhancement[19] and lithographically defined vortex pinning sites[20,21], the transmon circuit can be protected at magnetic fields relevant to these proposals, which approach and in some cases exceed 1 T[22–24].

In this work we report the integration of ballistic graphene JJs into microwave frequency superconducting circuits to create graphene based transmons. Using dispersive microwave spectroscopy we resolve the characteristic band dispersion of graphene, and observe coherent electronic interference effects that confirm the ballistic nature of our graphene JJs. We perform energy level spectroscopy at $B_{||} = 0$ T to resolve a linewidth of $\simeq 400$ MHz. Although the large linewidths prevent coherent qubit control, we demonstrate the device is insensitive to the applied magnetic field up to $B_{||} = 1$ T.

Results

Device structure. Figure 1a shows an optical microscope image of a typical graphene transmon device. It consists of four $\lambda/4$ coplanar waveguide (CPW) resonators multiplexed to a common feedline. Each resonator is capacitively coupled to a graphene transmon, with the graphene JJ being shunted by capacitor plates that provide a charging energy $E_C \simeq 360$ MHz. The resonators and capacitor plates are fabricated from 20 nm NbTiN due to its enhanced critical magnetic field[19], and we pattern the resonators with a lattice of artificial pinning sites to protect the resonator from resistive losses due to Abrikosov vortices[20,21]. The van der Waals pickup method is used to encapsulate monolayer graphene (G) between two hexagonal boron nitride (hBN) flakes and deposit it between the pre-fabricated capacitors plates (Fig. 1b)[7], before contacting the hBN/G/hBN stack by dry etching and sputtering MoRe. In this work, we present results from two graphene JJ transmon devices, with slightly different fabrication techniques. Device A uses a Ti/Au gate stack deposited directly on the hBN, before the junction is shaped via dry etching. Device B is shaped (Fig. 1c) before a Ti/Au gate stack with a SiN$_x$ interlayer is deposited (Fig. 1d).

Dispersive Fabry–Perot oscillations. We begin by performing spectroscopy of the resonator in device A as a function of the input power P_{in} (Fig. 2a). Varying the resonator's photon occupation from $\langle n_{ph} \rangle \simeq 1000$ to $\langle n_{ph} \rangle = 1$ we observe a dispersive shift $\chi = f_r - f_{bare}$ in the resonator frequency f_r from the high power value f_{bare}. This occurs due to a Jaynes-Cummings type interaction between the harmonic readout resonator and the anharmonic transmon spectrum, with the anharmonicity provided by the Josephson junction[25]. The magnitude of the shift $\chi = g^2/\Delta$ depends on the transmon-resonator coupling g, and the difference $\Delta = f_r - f_t$ between f_r and the ground state to first excited state transition frequency $f_t = E_t/h \simeq \sqrt{8E_JE_C}/h$, allowing us to infer E_J from χ[1]. Studying χ as a function of gate voltage V_G reveals the characteristic band dispersion of graphene (Fig. 2b) and allows the voltage at the charge neutrality point (CNP) V_{CNP} to be identified. At negative $V_G - V_{CNP}$, the chemical potential μ is below the CNP and the graphene is in the p-regime where holes are the dominant charge carrier. Deep into the p-regime, the high carrier density (n_C) gives a large E_J, placing f_t above the resonator and giving χ a small negative value (Fig. 2c). As V_G approaches the CNP, the Dirac dispersion minimises the density of states reducing E_J and f_t to a minimum. Since $\chi = g^2/\Delta$, as Δ approaches zero, χ diverges. Once on resonance, the resonator acquires some characteristic of the qubit, significantly broadening the lineshape. Simultaneously, the critical photon number $n_{Crit} = \Delta^2/4g^2$ collapses[26], moving the measurement into the 'transitionary' regime between high and low photon number as in Fig. 2a, causing the anomalous lineshapes visible in Fig. 2c near CNP. As V_G is increased past the CNP, n_{Crit} and the lineshapes recover, with electrons becoming the dominant charge carrier and E_J increasing to a maximum as expected from removal of the n-p-n junction formed by the contacts[7]. The p-regime also experiences periodic fluctuations in E_J as a function of V_G due to coherent electron interference effects in a Fabry–Perot cavity formed by n-p interfaces at the MoRe contacts[7]. Extracting a line

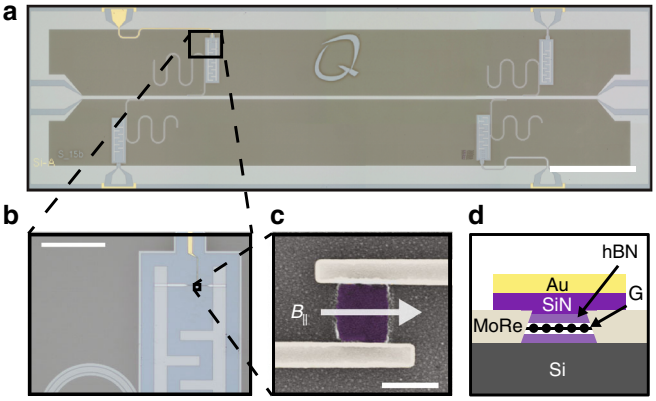

Fig. 1 Device structure **a** Optical image showing multiple CPW resonators frequency multiplexed to a common feedline (device B). Scale bar 1 mm. **b** Zoomed optical image of the capacitor plates that shunt the Josephson junction, with the gate, junction and contacts visible. Scale bar 100 μm. **c** SEM micrograph of a contacted boron nitride-graphene-boron nitride stack before fabrication of the gate. A magnetic field $B_{||}$ can be applied parallel to the film along the length of the junction contacts using a 3-axis vector magnet. Scale bar 500 nm. **d** Cross sectional diagram showing the fully contacted and gated stack

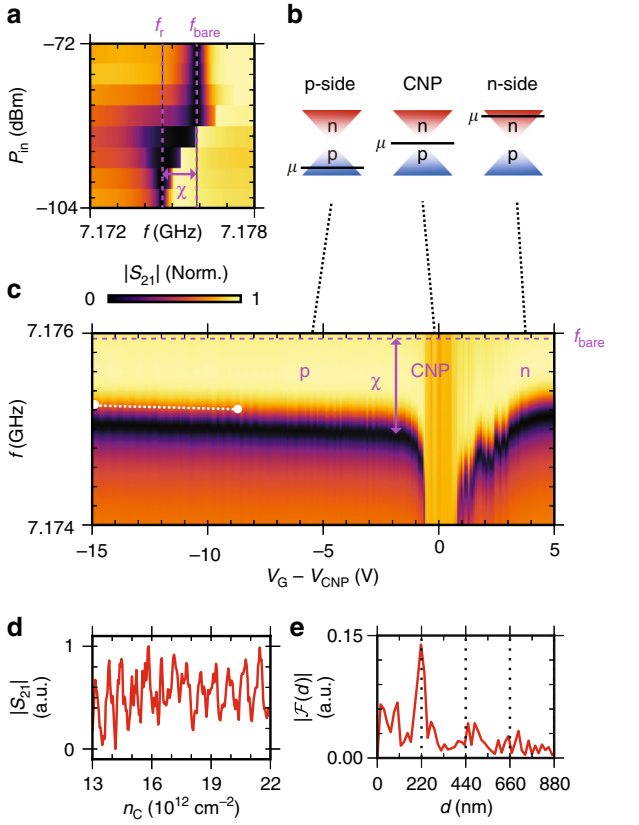

Fig. 2 Resonator spectroscopy as a function of P_{in} and V_G **a** $|S_{21}|$ (Norm.) as a function of input frequency f and input power P_{in}. At single photon occupancy the resonator experiences a frequency shift χ due to repulsion from an energy level above the resonator (device A). **b** Diagram of the Dirac cone band structure of graphene. Changing V_G to tune μ allows the dominant charge carriers to be varied between hole, charge neutral and electron-like regimes. **c** At single photon occupancy, $|S_{21}|$ (Norm.) is measured as f and V_G are varied, with the voltage at CNP ($V_{CNP} = 7.8$ V) subtracted. In the p-regime, χ oscillates as V_G is varied. We extract the charge carrier density n_c **d** from the white linecut to generate a Fourier transform **e** that is consistent with Fabry-Perot oscillations in a cavity of $d = 220$ nm

trace (white line Fig. 2c) to study the modulation in $|S_{21}|$ with n_C (Fig. 2d), and performing a Fourier transform (Fig. 2e) gives a cavity length of 220 nm in agreement with the device dimensions. The observation of a Dirac dispersion relation in combination with coherent electron interference effects confirm the successful integration of ballistic graphene JJs into a superconducting circuit.

Insensitivity to applied parallel magnetic field. In device B we observe additional coherent electronic interference effects in the form of universal conductance fluctuations (UCF)[14,27]. As we move from the p to the CNP regime, χ is seen to diverge repeatedly as f_t anti-crosses multiple times with f_r (Fig. 3a). This behaviour is repeated moving from the CNP to the n-regime, where E_J is again maximised. We demonstrate the field compatibility of the junction by applying a magnetic field $B_{||}$ along the length of the junction contacts, parallel to the plane of the film, using the resonator as a sensor for field alignment (see Supplementary Figs. 1 and 2 for alignment procedure details). Monitoring χ as $B_{||}$ is varied between 0 and 1 T (Fig. 3b) and calculating f_t (using $g = 43$ MHz, extracted from measurements in Fig. 4), demonstrates that χ and thus E_J are not significantly

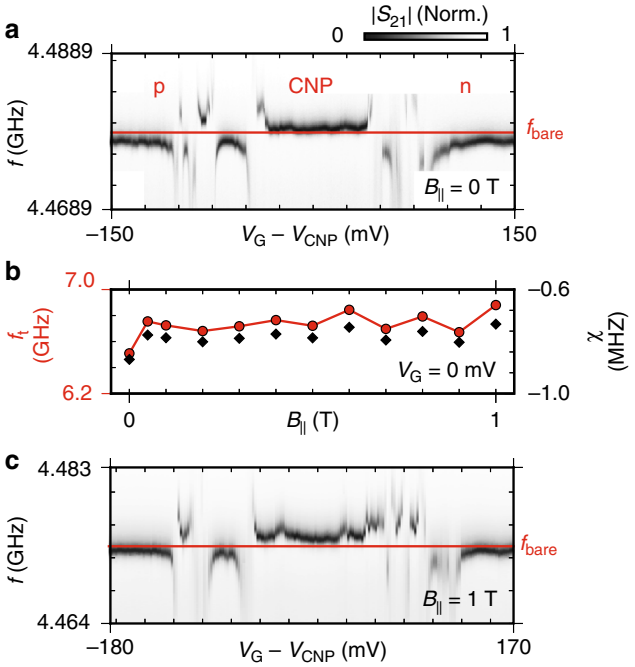

Fig. 3 Dispersive shift as a function of V_G and $B_{||}$ **a** At $B_{||} = 0$ T, $|S_{21}|$ (Norm.) versus f and V_G (with $V_{CNP} = 300$ mV subtracted) shows the symmetric band dispersion of graphene with additional fluctuations we attribute to UCF. **b** f_t (red circles) extracted from χ (black diamonds) versus $B_{||}$ at $V_G = 0$ V, showing f_t is not significantly affected. **c** Repeating **a** at $B_{||} = 1$ T with $V_{CNP} = 430$ mV subtracted confirms the graphene JJ behaves equivalently to $B_{||} = 0$ T. The variation observable in b and shift in V_{CNP} between a and c we attribute to slow gate drift

affected by the applied $B_{||}$. The small amount of variation observed is attributed to charge noise induced gate drift which was observed throughout the duration of the experiment. Studying χ as a function of V_G at $B_{||} = 1$ T (Fig. 3c) again reveals the characteristic Dirac dispersion as seen in Fig. 3a, with modified UCF and shifted V_{CNP} due to slow gate drift. The insensitivity of f_t to applied field and similarity of device operation at $B_{||} = 0$ and 1 T confirm the field resilience of both the graphene JJ and superconducting circuit.

Two tone spectroscopy in high parallel magnetic fields. In order to better understand the microwave excitation spectra of our system we proceed to measure it directly via two-tone spectroscopy[1]. The readout tone is set to f_r whilst a second tone f_d is used to drive the circuit. Excitation of the system results in a state dependent shift of the resonator frequency, and is detected by measuring the change in the complex transmission S_{21} at f_r. At $V_G = 0$ V (p-regime), two-tone spectroscopy at $B_{||} = 0$ and 1 T (Fig. 4a) can be fitted with a Lorentzian to extract the transmon transition $f_t \simeq 5.2$ GHz and transition linewidth $\gamma \simeq 400$ MHz. At $B_{||} = 1$ T, f_t and thus E_J differ only slightly with γ increasing slightly from 350 to 425 MHz. The transmon resonator coupling $g = \sqrt{\chi\Delta} = 43$ MHz is extracted from the observed dispersive shift χ and detuning Δ, and used in the calculation of f_t in Fig. 3. We attribute the change in f_t from Fig. 3b and the large γ to the dielectric induced charge noise mentioned previously. An estimate of $E_J = 40.2$ μeV $= 9.72$ GHz can be provided using the relation $E_t = hf_t \simeq \sqrt{8E_JE_C}$. Performing two-tone spectroscopy in the n-regime while tuning V_G reveals a gate-tunable energy level that is visible above and below the resonator (Fig. 4b, V_{CNP}

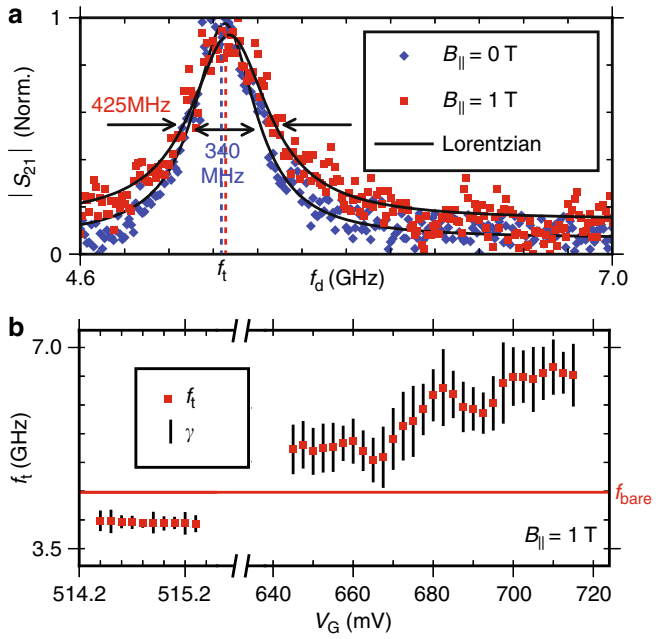

Fig. 4 Two tone spectroscopy **a** Normalised $|S_{21}|$ at f_r as f_d is varied can be fitted to extract f_t and γ at $V_G = 0$ V. At $B_{||} = 1$ T, γ shows a 25% increase compared to $B_{||} = 0$ T. **b** At $B_{||} = 1$ T, f_t and γ are extracted as V_G is varied, demonstrating f_t can be swept over a wide frequency range. Lines bisecting each f_t are not error bars, but represent the extracted γ at each f_t

not specified due to gate drift during measurement) that can be fitted to extract f_t and γ, giving a minimum linewidth of 166 MHz (see Supplementary Fig. 3 for the raw data).

Discussion

The observation of a transition and the inferred high value of E_J in the n and p-regimes (Fig. 4a) provides additional confirmation of the electron-hole symmetry expected in graphene. Additional measurement of the higher order two-photon f_{02} transition would allow for exact measurements of E_J and E_C via diagonalisation of the Hamiltonian, enabling investigations into mesoscopic effects of interest in graphene JJs[28,29]. Importantly, the transition and thus E_J can be varied over a wide frequency range, satisfying a key requirement for implementation into topological QC proposals[3]. If graphene based transmons are to be successfully implemented into these proposals however, the large linewidths that currently prevent measurements of relaxation and coherence lifetimes (T_1, T_2^*) must be reduced. We believe that material improvements to the dielectric materials can achieve this.

In conclusion, we have integrated a graphene JJ into a superconducting circuit to make a graphene based transmon. Additionally, we have achieved operation at $B_{||} = 1$ T, a magnetic field more than an order of magnitude higher than previous studies[16,30]. While the broad linewidths prevented the demonstration of coherent qubit control, these results establish graphene based microwave circuits as a promising tool for topological and hybrid QC schemes, and for probing mesoscopic phenomena of interest at high magnetic fields.

Methods

Sample fabrication. To fabricate the two devices (A and B) 20 nm of NbTiN is sputtered onto intrinsic Si wafers in an Ar/N atmosphere. The resonators, feedline and transmon are reactive ion etched in an SF_6/O_2 atmosphere. In this etching step, an array of artificial pinning sites is also defined. Monolayer graphene is encapsulated between two hBN flakes ($t \simeq 15$ nm each), then deposited between pre-fabricated capacitors using a PMMA based van der Waals pickup method. Contact to the graphene stack is made by etching in a CHF_3/O_2 environment, followed by sputtering MoRe ($t = 80$ nm). As shown in Supplementary Fig. 4, device A was contacted to give a junction length of 300 nm. A Ti/Au top gate is then sputtered on top of the stack. The device is then shaped in a CHF_3/O_2 plasma to be 1000×300 nm^2 in size. Device B was contacted to provide a junction length of 500 nm. The long thin leads were geometrically restricted in two dimensions, making it less favourable for vortices to form, protecting the superconductivity of the contacts proximitising the junction. The junction is then shaped in a CHF_3/O_2 plasma to be 500×500 nm^2. A SiN_x/Ti/Au top gate stack is then sputtered to give full junction coverage, giving greater control of μ in the junction.

Sample characterisation. All measurements were performed in a dilution refrigerator with a base temperature of 15 mK. The samples were enclosed in a light tight copper box, and thermally anchored to the mixing chamber. An external magnetic field is applied to the sample using a 3-axis vector magnet. The two different measurement configurations used in this manuscript are depicted in Supplementary Fig. 5. Two coaxial lines and one DC line were used to control the sample. The sample was connected to the DC voltage source by a line that was thermally anchored at each stage and heavily filtered at the mixing chamber by low frequency RC, π and copper powder filters. The line used to drive the feedline input was heavily attenuated to reduce noise and thermal excitation of the cavity, allowing the single photon cavity occupancy to be reached. The output line of the feedline was connected to an isolator (Quinstar QCI-080090XM00) and circulator (Quinstar QCY-060400CM00) in series to shield the sample from thermal radiation from the HEMT amplifier (Low Noise Factory LNF-LNC4-8_C) on the 4 K stage. Resonator spectroscopy of device A was performed using circuit (a) to measure the amplitude and phase response of the complex transmission S_{21} as the frequency was varied. Resonator and two-tone spectroscopy of device B was performed using circuit (b), with a splitter used to combine the readout and excitation tones. This allows the complex S_{21} to be measured, but only at fixed resonator readout frequency otherwise only $|S_{21}|$ can be recorded.

Data availability

The data used to support this study, and the code used to generate the figures are available from a public data repository here https://doi.org/10.4121/uuid:b7340d11-e47e-44eb-a60d-679d758c7160. (ref. [31]).

Received: 16 July 2018 Accepted: 18 October 2018
Published online: 05 November 2018

References

1. Koch, J. et al. Charge-insensitive qubit design derived from the Cooper pair box. *Phys. Rev. A.* **76**, 042319 (2007).
2. Hassler, F., Akhmerov, A. R. & Beenakker, C. W. J. The top-transmon: a hybrid superconducting qubit for parity-protected quantum computation. *New J. Phys.* **13**, 095004 (2011).
3. Hyart, T. et al. Flux-controlled quantum computation with Majorana fermions. *Phys. Rev. B* **88**, 035121 (2013).
4. Aasen, D. et al. Milestones toward Majorana-based quantum computing. *Phys. Rev. X* **6**, 031016 (2016).
5. Kubo, Y. et al. Hybrid quantum circuit with a superconducting qubit coupled to a spin ensemble. *Phys. Rev. Lett.* **107**, 220501 (2011).
6. Ranjan, V. et al. Probing dynamics of an electron-spin ensemble via a superconducting resonator. *Phys. Rev. Lett.* **110**, 067004 (2013).
7. Calado, V. E. et al. Ballistic Josephson junctions in edge-contacted graphene. *Nat. Nanotechnol.* **10**, 761–764 (2015).
8. Van Woerkom, D. J., Geresdi, A. & Kouwenhoven, L. P. One minute parity lifetime of a NbTiN Cooper-pair transistor: Supplementary Information. *Nat. Phys.* **11**, 547–550 (2015).
9. Kurizki, G. et al. Quantum technologies with hybrid systems. *Proc. Natl Acad. Sci.* **112**, 3866–3873 (2015).
10. Ristè, D. et al. Millisecond charge-parity fluctuations and induced decoherence in a superconducting transmon qubit. *Nat. Commun.* **4**, 1913 (2013).
11. Doh, Y. et al. Applied physics: tunable supercurrent through semiconductor nanowires. *Science* **309**, 272–275 (2005).
12. Van Woerkom, D. J. et al. Microwave spectroscopy of spinful Andreev bound states in ballistic semiconductor Josephson junctions. *Nat. Phys.* **13**, 876–881 (2017).
13. Hays, M. et al. Direct microwave measurement of Andreev-bound-state dynamics in a semiconductor-nanowire josephson junction. *Phys. Rev. Lett.* **121**, 047001 (2018).

14. De Lange, G. et al. Realization of microwave quantum circuits using hybrid superconducting-semiconducting nanowire Josephson elements. *Phys. Rev. Lett.* **115**, 127002 (2015).
15. Larsen, T. W. et al. Semiconductor-nanowire-based superconducting qubit. *Phys. Rev. Lett.* **115**, 127001 (2015).
16. Luthi, F. et al. Evolution of nanowire transmon qubits and their coherence in a magnetic field. *Phys. Rev. Lett.* **120**, 100502 (2018).
17. Allen, M. T. et al. Observation of electron coherence and Fabry-Perot standing waves at a graphene edge. *Nano. Lett.* **17**, 7380–7386 (2017).
18. Chtchelkatchev, N. M. & Burmistrov, I. S. Conductance oscillations with magnetic field of a two-dimensional electron gas superconductor junction. *Phys. Rev. B* **75**, 214510 (2007).
19. Stan, G., Field, S. B. & Martinis, J. M. Critical field for complete vortex expulsion from narrow superconducting strips. *Phys. Rev. Lett.* **92**, 97003–97004 (2004).
20. Bothner, D., Gaber, T., Kemmler, M., Koelle, D. & Kleiner, R. Improving the performance of superconducting microwave resonators in magnetic fields. *Appl. Phys. Lett.* **98**, 102504 (2011).
21. Kroll, J. G. et al. Magnetic field resilient superconducting coplanar waveguide resonators for hybrid cQED experiments. Preprint at http://arxiv.org/abs/1809.03932 (2018).
22. Deng, M. T. et al. Majorana bound state in a coupled quantum-dot hybrid-nanowire system. *Science* **354**, 1557–1562 (2016).
23. Suominen, H. J. et al. Zero-energy modes from coalescing Andreev states in a two-dimensional semiconductor-superconductor hybrid platform. *Phys. Rev. Lett.* **119**, 176805 (2017).
24. Zhang, H. et al. Quantized Majorana conductance. *Nature* **556**, 74–79 (2018).
25. Reed, M. D. et al. High-fidelity readout in circuit quantum electrodynamics using the Jaynes-Cummings nonlinearity. *Phys. Rev. Lett.* **105**, 173601 (2010).
26. Schuster, D. I. *Circuit Quantum Electrodynamics*. Ph.D. thesis, Yale University (2007).
27. Lee, P. A. & Stone, D. A. Universal conductance fluctuations in metals. *Phys. Rev. Lett.* **55**, 1622–1625 (1985).
28. Nanda, G. et al. Current-phase relation of ballistic graphene Josephson junctions. *Nano. Lett.* **17**, 3396–3401 (2017).
29. Kringhøj, A. et al. Anharmonicity of a superconducting qubit with a few-mode Josephson junction. *Phys. Rev. B* **97**, 060508 (2018).
30. Ku, J., Yoscovits, Z., Levchenko, A., Eckstein, J. & Bezryadin, A. Decoherence and radiation-free relaxation in Meissner transmon qubit coupled to Abrikosov vortices. *Phys. Rev. B* **94**, 165128 (2016).
31. Kroll, J. G. et al. Field compatible circuit quantum electrodynamics with graphene Josephson junctions. 4TU. Research Data. https://doi.org/10.4121/uuid:b7340d11-e47e-44eb-a60d-679d758c7160 (2018).

Acknowledgements

We thank D.J. van Woerkom for fabrication assistance, M.W.A. de Moor and A. Proutski for helpful discussion and L. DiCarlo, C. Dickel and F. Lüthi for experimental advice and software support. This work was supported by the European Research Council (ERC), The Dutch Organisation for Scientific Research (NWO), and Microsoft Corporation Station Q.

Author contributions

K.W. and T.T. grew the hBN crystals, J.G.K. and W.U. fabricated the devices, J.G.K., K.L. v.d.E. and D.d.J performed the measurements and J.G.K. and K.L.v.d.E. analysed the measurements. The manuscript was prepared by J.G.K. with K.L.v.d.E., S.G., M.C.C. and L.P.K. providing input. S.G., M.C.C. and L.P.K. supervised the project.

Additional information

Supplementary Information accompanies this paper at https://doi.org/10.1038/s41467-018-07124-x.

Competing interests: The authors declare no competing interests.

Reprints and permission information is available online at http://npg.nature.com/reprintsandpermissions/

Publisher's note: Springer Nature remains neutral with regard to jurisdictional claims in published maps and institutional affiliations.

Open Access This article is licensed under a Creative Commons Attribution 4.0 International License, which permits use, sharing, adaptation, distribution and reproduction in any medium or format, as long as you give appropriate credit to the original author(s) and the source, provide a link to the Creative Commons license, and indicate if changes were made. The images or other third party material in this article are included in the article's Creative Commons license, unless indicated otherwise in a credit line to the material. If material is not included in the article's Creative Commons license and your intended use is not permitted by statutory regulation or exceeds the permitted use, you will need to obtain permission directly from the copyright holder. To view a copy of this license, visit http://creativecommons.org/licenses/by/4.0/.

© The Author(s) 2018